Research Article

Flexibility-Patterned Liquid-Repelling Surfaces

Songtao Hu,[||] Xiaobao Cao,[||] Tom Reddyhoff, Xi Shi,* Zhike Peng,* Andrew J. deMello, and Daniele Dini

Read Online

ACCESS | Metrics & More | Article Recommendations | Supporting Information

ABSTRACT: Droplets impacting solid surfaces is ubiquitous in nature and of practical importance in numerous industrial applications. For liquid-repelling applications, rigidity-based asymmetric redistribution and flexibility-based structural oscillation strategies have been proven on artificial surfaces; however, these are limited by strict impacting positioning. Here, we show that the gap between these two strategies can be bridged by a flexibility-patterned design similar to a trampoline park. Such a flexibility-patterned design is realized by three-dimensional projection micro-stereolithography and is shown to enhance liquid repellency in terms of droplet impalement resistance and contact time reduction. This is the first demonstration of the synergistic effect obtained by a hybrid solution that exploits asymmetric redistribution and structural oscillation in liquid-repelling applications, paving the rigidity−flexibility cooperative way of wettability tuning. Also, the flexibility-patterned surface is applied to accelerate liquid evaporation.

KEYWORDS: *artificial surface, droplet impact, liquid repellency, liquid evaporation, 3D printing*
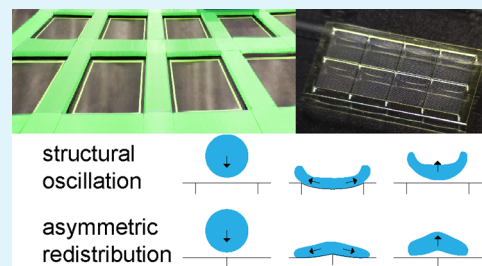
1. INTRODUCTION

Understanding and controlling droplet−solid impacting behaviors has attracted substantial attention in various technological applications, including liquid-repelling,[1] self-cleaning,[2] inkjet printing,[3] and energy harvesting.[4] Taking advantage of the recent advances in surface micronanofabrication on both morphological and chemical attributes, unprecedented progress has been made in elevating the liquid-repelling ability in terms of impalement resistance (regulating the outcomes of impacting events from pinning to bouncing) and contact time (reducing the droplet−solid contact time at impact). Normally, impinging droplets can bounce off a super-repellent (large contact angle but tiny adhesion) surface after the retracting motion with a circular symmetry, resulting in the contact time bounded below by an inertia−capillarity limit.[5] As the above limit relies on symmetrical bouncing, the introduction of asymmetry from surface curvatures has been shown to induce a measurable reduction in contact time.[6−11]

Despite this, the asymmetric bouncing urges a strict alignment between impinging droplets and surface curvatures. In contrast with the above solutions, which are constrained by a rigid setting, flexible surfaces inspired by natural leaves and wings have been suggested to rebound impinging droplets before a full retraction with the use of structural oscillations at impact, thus shifting the research focus from statics to dynamics.[12−16] However, this contact time reduction still depends on impacting positioning, thus recommending the flexibilization of micro-substructures on surfaces, which relies on the high uniformity of surface micronanofabrication.[17−20]

Here, we report a flexibility-patterned surface (FPS), a matrix of flexible cells barred by rigid edges similar to a trampoline park (see Figure 1a), for liquid-repelling application through combining the two aforementioned strategies (i.e., rigidity-based asymmetric redistribution and flexibility-based structural oscillation). Using three-dimensional printing, we realize the FPS and verify its liquid repellency enhancement in terms of droplet impalement resistance and contact time reduction. We believe this study to be the very first demonstration of the synergistic effect obtained by a hybrid strategy in liquid-repelling applications, providing an unprecedented level of control over wettability. Also, the FPS is applied to accelerate liquid evaporation.

2. EXPERIMENTAL SECTION

2.1. Surface Fabrication. A 10 μm thick liquid film made of a flexible UTL photosensitive resin (BMF Precision Technology Co., Ltd., China) was spread over an indium-tin-oxide-coated fused silica on a spin coater (see Figure S1). Three-dimensional projection micro-stereolithography was conducted on a nanoArch S140 system (BMF Precision Technology Co., Ltd., China) to cure the resin, fabricating the designed grids. The grids were rinsed and then repositioned in the nanoArch system. After the introduction of a liquid rigid HTL photosensitive resin (BMF Precision Technology Co., Ltd., China),
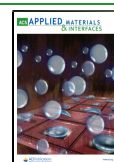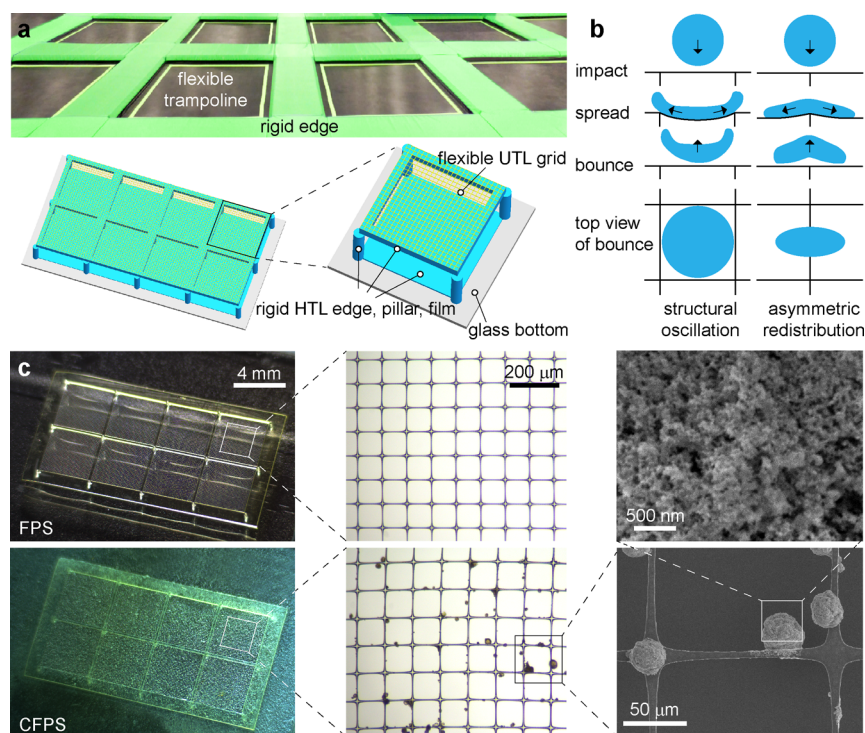
Figure 1. FPSs and droplet impact dynamics. (a) Schematic of a trampoline park-inspired FPS. (b) Schematic of two mechanisms utilized by the FPS to control droplet impact dynamics. (c) Optical and scanning electron microscopic images of the FPS realized by three-dimensional printing, together with a CFPS sprayed with low-surface-energy particles.

the printer was used to fabricate the designed edges and pillars. The resulting fabrication was rinsed, turned upside down, and then attached to another indium-tin-oxide-coated fused silica with a liquid HTL film. After UV treatment, the HTL film was cured to strengthen the adhesion between the pillars and the bottom fused silica. Due to the adhesion difference, the top fused silica was easily separated from the grids, forming the designed FPS. Commercial low-surface-energy particles, Ultra-Ever Dry (UltraTech International Inc., USA),[2,21,22] were sprayed to yield a coated FPS (CFPS).

2.2. Morphology Characterization. Morphological images of surfaces were taken with an optical microscope LW300LMDT (Cewei Guangdian, China) and a scanning electron microscope Sirion 200 (Philips, USA) accounting for a multiscale requirement.

2.3. Liquid-Repelling Test. *2.3.1. Static Liquid Repellency Test.* A microsyringe needle was used to compress the surface grids lightly and heavily on an optical microscope LW300LMDT (Cewei Guangdian, China) to investigate the mechanics. Also, the contact angle and adhesion of 2 μL deionized water droplets in relation to the surfaces were investigated on a contact angle goniometer SDC-100 (SINDIN, China) in sessile drop mode under a controlled temperature (25 °C) and relative humidity (45%). For contact angle measurements, the characterization was conducted 30 s after the droplets contacted the surfaces to ensure equilibrium. Three measurements were performed for each surface for repeatability analysis.

2.3.2. Kinetic Liquid Repellency Test. The impacting behaviors of 8 μL deionized water droplets on the surfaces were recorded by a high-speed camera FASTCAN SA1.1 (Photron USA Inc., USA) at a rate of 5000 fps. An electrically controlled microsyringe pump was used to release droplets at a specified height. Three measurements were performed for each surface at each releasing height. For each surface, the measurement was stopped when pinning behaviors appeared twice. To discuss the influence of the relationship between flexible cell size and droplet size, the above impacting tests were repeated for 0.5 μL deionized water droplets.

2.4. Evaporation Test. A micropipette was used to generate 2 μL deionized water droplets to lightly touch the surfaces on an optical

microscope LW650LJT (Cewei Guangdian, China), allowing the exploration of evaporation behaviors.

3. RESULTS AND DISCUSSION

3.1. Design and Fabrication. Inspired by a trampoline park, we designed a FPS as a matrix of flexible cells barred by rigid edges (see Figure 1a). As per previous works, a reduction in contact time is envisioned to be triggered by the asymmetric redistribution mechanism when a droplet impacts a rigid edge that exhibits a convex curvature together with the deformed neighboring flexible cells (see right part of Figure 1b)[6−11] and will be transferred to the structural oscillation mechanism when the impact occurs on a flexible cell (see left part of Figure 1b).[12−20]

To realize our design (see Figure 1c), three-dimensional printing based on projection micro-stereolithography was conducted on a nanoArch S140 system (BMF Precision Technology Co., Ltd., China) because it has been proved as an industrial microprecision printer to rapidly tailor stereo-structures, shedding light on wettability studies.[23,24] On the FPS, flexible grids made of a UTL photosensitive resin (BMF Precision Technology Co., Ltd., China) were supported and barred by underlying rigid edges made of a HTL photo-sensitive resin (BMF Precision Technology Co., Ltd., China), which were connected to an indium-tin-oxide-coated fused silica through rigid HTL pillars. An additional HTL film was introduced to strengthen the mechanical resistance to shear loads at the pillar bottom,[25] as well as to enhance the adhesion between the pillars and the substrate required by surface fabrication (see Figure S1). The diameter and the pitch of flexible grids were set to 10 and 100 μm, respectively; the side length and the pitch of rigid edges were set to 200 and 4000 μm, respectively; and the diameter and the height of rigid pillars were set to 250 and 1000 μm, respectively. Although a
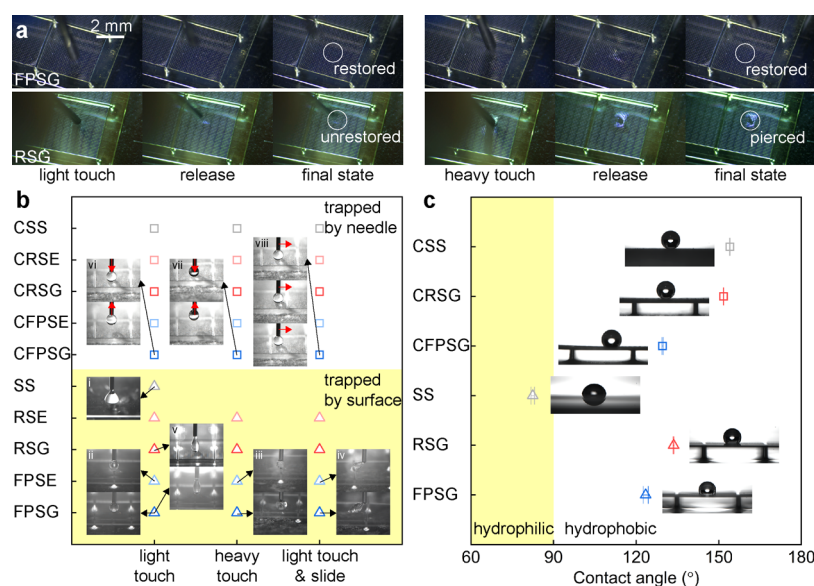
Figure 2. Static liquid repellency. (a) Mechanics of the fabricated surfaces under light and heavy compressions on an optical microscope. (b,c) Contact angle and adhesion of water droplets lightly touching, heavily touching, and sliding over the fabricated surfaces on a contact angle goniometer.

grid topology has been previously demonstrated to improve liquid repellency solely from the morphological point of view,[26] we further sprayed the FPS with low-surface-energy particles to yield a CFPS (Figure 1c)[2,21,22] because in this study we mainly focused on the kinetic repellency to extreme conditions with impacting pressure. The surfaces were purposely designed as a matrix consisting of 2 × 4 cells due to the block size (19.2 × 10.8 mm²) of the printer and to allow a clear recording of the droplet−solid impacting behaviors. However, it should be noted that it would be simple to extend the horizontal size of our surfaces on the nanoArch system via splicing for industrial applications.

Also, we fabricated the corresponding rigid cases [rigid surface (RS) and coated RS (CRS) on which the UTL grids were substituted by the HTL ones] and smooth cases [smooth surface (SS) and coated smooth surface (CSS) which were made of the UTL resin] as references (see Figure S2). Hereafter, the grid and edge regions of the FPS, RS, CFPS, and CRS are referred to as FPSG, FPSE, RSG, RSE, CFPSG, CFPSE, CRSG, and CRSE.

3.2. Static Liquid Repellency. We first investigated the mechanics of the fabricated surfaces by compression tests on an optical microscope (see Movie S1). When the needle of a microsyringe lightly touched the FPSG and RSG, the contacting grids deformed in a downward direction (see Figure 2a). After releasing the compressing load, the deformation was eventually restored on the FPSG but retained on the RSG. Even if the RSG was pierced by the needle under a heavy load, the restoring capacity still held on the FPSG, demonstrating the flexibility endowed by the soft, tough UTL resin.

We further investigated the static liquid repellency of the fabricated surfaces by lightly touching, heavily touching (i.e., continue to press the droplet after the droplet−surface contact), and sliding over hanging water droplets on a contact angle goniometer in terms of contact angle and adhesion (see Movie S2). When the SS lightly touched the droplet, the droplet showed a rapidly symmetrical spreading on the surface and was then trapped by the surface (see i, Figure 2b),

indicating the inherent hydrophilicity of the UTL resin. However, the droplet beaded up on the FPSG and FPSE under light (see ii, Figure 2b) and heavy (see iii, Figure 2b) loads and was eventually trapped by the surface. The former beading behavior indicates the static repellency that results from air pockets beneath the droplet, which connect to the atmosphere, so that the droplet is suspended solely by surface tension, regardless of the additional pressure from trapped air. The latter trapping behavior is due to wetting behaviors occurring within partial grids, which can also be evidenced by the adhesive behavior when the FPSG and FPSE were slid over the droplet (see iv, Figure 2b), confirming large values for both the contact angle and adhesion, consistent with the petal effect.[27−29] Similar phenomena can be observed on the RSG and RSE, except for the undeformed response to droplet touching, leaving (see v, Figure 2b), and sliding due to the rigidity of the HTL resin. With the low-surface-energy chemical modification, the surfaces in the coated series left the droplet to the needle after light touching (see vi, Figure 2b), heavy touching (see vii, Figure 2b), and sliding (see viii, Figure 2b), indicating a super repellence consisting of a large contact angle and tiny adhesion. Also, we quantified the values of the contact angle, as depicted in Figure 2c. Note that the quantification was only performed for the grid series because the edge series exhibited a directional wetting,[21] and the quantification for the coated grid series was conducted by dripping the droplet from a micropipette with a very low velocity because a hanging droplet cannot be directly trapped by the coated surfaces. The FPSG and RSG exhibited contact angles of 123.42 and 133.60°, respectively, in comparison to the value of 82.42° on the SS, thereby demonstrating a drastic transformation of static liquid repellency from inherent hydrophilicity to structural hydrophobicity with the assistance of a grid topology. This transformation was also achieved by the low-surface-energy chemical modification (SS vs CSS). Also noteworthy is the observation that the contact angle decreased mildly when the surfaces changed from being rigid to flexible (RSG vs FPSG; CSS vs CRSG vs CFPSG), which seems to imply a weakened repellence. However, it should be
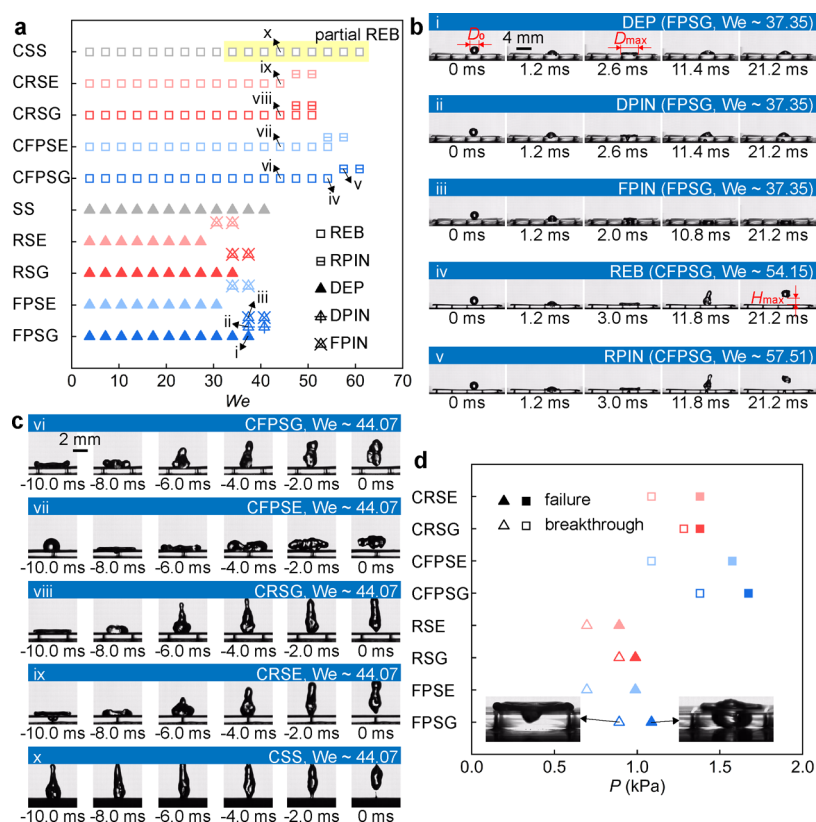
Figure 3. Impalement resistance. (a) Outcomes of water droplets impacting the fabricated surfaces as a function of *We*. (b) Snapshots exemplarily provided to visualize different impacting outcomes over time. (c) Snapshots exemplarily provided to visualize different bouncing types over time. (d) Breakthrough and failure limits of the fabricated surfaces.

highlighted that the contact angle is a macroscopic index based on a specified baseline, so that the partial deformation of flexible grids will spontaneously characterize a reduced value to underestimate the real static repellency (see Figure S3).

3.3. Kinetic Liquid Repellency. After the static liquid repellency investigation, we conducted impacting tests to gauge the kinetic repellency of the fabricated surfaces to water droplets with different impinging velocities (see Movies S3 and S4).

3.3.1. Impalement Resistance. Figure 3a presents the outcomes of impacting events along with an increased Weber (*We*) number (see Table S1), which is nondimensionalized as $D_0 \rho V_0^2 / \sigma$ to quantify the ratio between the inertial and capillary forces. Here, ρ and σ are the density and tension of a droplet; D_0 and V_0 are the diameter and velocity of a droplet in flight before the contacting instant. Referring to the definitions of the Wenzel and the Cassie−Baxter wetting states for hierarchical surfaces,[30,31] we have defined the outcomes in this study as follows. For depositing (see DEP, i, Figure 3b), the impinging droplet spreads to the maximum diameter D_{max}, retracts, and is eventually trapped by the grids and edges, thus yielding the Cassie−Baxter wetting state. Notably, the DEP behavior can be classified into two types: at small *We*, as the impacting pressure is lower than the breakthrough limit,[32] the droplet cannot impale the defense of grids; at large *We*, even if the impacting pressure exceeds the breakthrough limit, the droplet impales the grids but restores back again as the additional space provided by the rigid pillars prevents the contact between the impaled droplet and the substrate. As this space is restricted by the height of the rigid pillars, it is also possible for a droplet with a large impacting velocity to impale

the grids and then touch the substrate so as to enter the Wenzel wetting state, defined as pinning. Specifically, for depositing-pinning (see DPIN, ii, Figure 3b), the lower part of the droplet is trapped by the substrate while the upper part is prevented by the grids and edges so as to form a DEP consequence; for full pinning (see FPIN, iii, Figure 3b), the entire droplet impales the grids and is completely trapped by the substrate. With regard to rebounding (see REB, iv, Figure 3b), the surface renders a bouncing response to impinging droplets. Similarly, when a droplet has a large velocity as it touches the substrate, another type of pinning will inherit the place of the REB, with the lower part being trapped by the substrate but the upper part rebounding, defined as rebounding-pinning (see RPIN, v, Figure 3b). Note that, in this study, the defined RPIN, DPIN, and FPIN are regarded as a failure of impalement resistance. The clear version of Figure 3b can be found in Figure S4.

For the uncoated series, the DEP response of the surface to impinging droplets was substituted by the DPIN or the FPIN as the value of *We* increased. FPSG and FPSE rendered the above transformation when *We* increased to ~37.35 and ~33.99, respectively, greater than the values of ~33.99 and ~30.63 for the RSG and RSE, highlighting the superior impalement resistance endowed by structural oscillations (see Movie S5). However, as no bouncing response was observed, the entire uncoated series exhibited a nonideal kinetic repellence to resist impinging droplets. With regard to the coated series, the REB behavior was initially observed, changing to the RPIN as *We* increased. Notably, the CSS started to exhibit a partial REB when *We* exceeded ~30.63 (see Figure S5), failing with respect to impalement resistance.[12] As
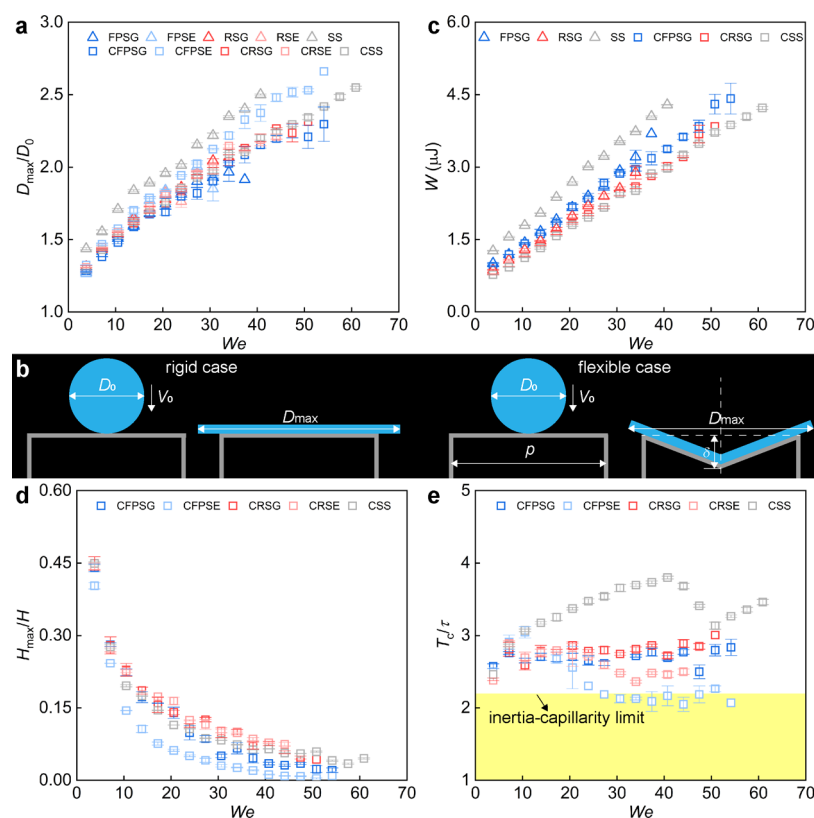
Figure 4. Droplet impact dynamics. (a) Maximum spreading factor D_{max}/D_0 as a function of We. (b,c) Theoretical spreading model to estimate the work done W in spreading and the corresponding results as a function of We. (d) Restitution coefficient H_{max}/H as a function of We. (e) Dimensionless contact time T_c/τ as a function of We, together with the theoretical inertia−capillarity limit $T_c/\tau = 2.2$.

the REB−RPIN transformation occurred on the CRSG and CRSE when We reached ~47.43, the enhancement of impalement resistance provided by a grid topology can be quantified as 54.85%. More interestingly, the occurrence of the REB−RPIN transformation on the CPFSG ($We \sim 57.50$) and CPFSE ($We \sim 54.15$) was significantly later than that on the CRSG and CRSE. Accordingly, it can be concluded that the impalement resistance has been elevated by 21.23 and 14.17% through the structural oscillation and asymmetric redistribution mechanisms, respectively.

We further subdivided the types of bouncing droplets (see Figures 3c and S6). To facilitate the comparison, we set the bouncing instant to be zero and presented prebouncing images every 2 ms. The rigid series (CRSG, CRSE, and CSS) exhibited similar bouncing behaviors. More precisely, the impacting droplets spread to a pancake shape to trigger the retracting motion[33,34] and then left the surface after a thorough retraction to a bowling-pin-like shape (see viii, ix and x, Figure 3c). The time between retracting and rebounding on the CSS was significantly longer than that on the other two. Diversely, the impinging droplet on the CFPSG exhibited an upturned outermost rim for the spread pancake and left the surface after a full retraction (see vi, Figure 3c). Of note, this unusual bouncing shape is at odds with the oscillation-based bouncing (a pancake shape with an upturned outermost rim, as shown in the left part of Figure 1b).[12−16] This is induced by the confined oscillation space for flexible grids or the wetting within the contacting grids. Gratifyingly, the impinging droplet on the CFPSE exhibited a downturned outermost rim for the spread film and took off with an incomplete retraction (see vii, Figure 3c), in good agreement with the droplet bouncing on a convex

surface (see the right part of Figure 1b).[8] Obviously, the droplet on the CFPSE took a significantly shorter time to bounce because of an asymmetric momentum and mass redistribution.[8]

Here, the bouncing type on the grids of the FPS (see vi, Figure 3c) is criticized for its deviation from the initial envisioning (a pancake bouncing with an upturned outermost rim, as shown in the left part of Figure 1b). As previously mentioned, this can be induced by confined oscillation and partial wetting for flexible grids. Referring to previous studies on flexible dewetting, the amplitude of structural oscillations should be at least 200 μm,[12−20] which is the case in the current study (see Figure S7), thus recommending the later influence factor. We selected a grid topology because similar microstructures have been shown to improve liquid repellency.[26] To address the grid wetting issue, an alternative is to substitute the grid topology with a solid film. However, an additional risk should be carefully considered: it is possible for a solid film to render an impalement resistance failure in the form of partial bouncing, even more readily than a grid topology (see Figure 3a). Therefore, a better choice is to further optimize the grid geometry (e.g., changing the diameter and pitch or adding hierarchical structures) to weaken the water-trapping capacity, calling for a thorough parametric study.

We then compared the breakthrough and failure limits of the fabricated surfaces to highlight the importance of the safety space reserved by the rigid pillars (see Figure 3d). At impact, the impacting load between the droplet and the surface can be estimated as $0.25\pi\rho D_0^2 V_0^2$,[35] which can be understood as an impacting pressure $P = \rho V_0^2$ over an area of $0.25\pi D_0^2$. Accordingly, we defined the breakthrough limit and failure

limit as the values of P on the first occurrences of droplet impaling and pinning, respectively. On the surface, the edge region more favorably encountered droplet breakthrough and failure than the grid region. With the low-surface-energy chemical modification, thresholds for droplet impaling and pinning were significantly improved. Interestingly, the surface flexibilization significantly increased the failure limit, but negligibly affected the breakthrough limit, indicating that the surface flexibilization improved the impalement resistance by weakening secondary impaling behaviors. Also noteworthy is the role that rigid supports play in droplet impact. First, the rigid pillars provide oscillation space for the flexible grids, which is the precondition for a flexible setting. Second, when the impacting pressure is higher than the breakthrough limit, a droplet will impale the defense of grids. The rigid pillars, therefore, reserve additional safety space to avoid contact between the impaled droplet and the substrate, yielding a difference between the breakthrough and failure limits. This appears to suggest rigid supports to be designed as high as possible. However, an extremely large height may introduce new challenges to rigid supports, for example, robustness to shear loads.

In addition, we discussed the influence of the relationship between flexible cell size and droplet size on impalement resistance by reducing the droplet volume from 8 to 0.5 μL (see Table S1). The occurrence of the REB−RPIN transformation on the CPFSG ($We \sim 49.61$) was later than that on the CRSG ($We \sim 38.92$), indicating a 27.47% enhancement through the structural oscillation mechanism, consistent with the conclusion of 21.23% drawn from the 8 μL droplet experiment above. However, the asymmetric redistribution mechanism was not triggered on the CFPSE in comparison to the CRSE and the CSS due to the small droplet size with respect to rigid edges.

3.3.2. Spreading Performance. Figure 4a presents the maximum spreading factor D_{max}/D_0 of water droplets impacting the fabricated surfaces as a function of We (see Figure S8). The FPS and RS exhibited overlapped D_{max}/D_0 which was much smaller than that of the SS, highlighting the dewetting property endowed by a grid topology. In the coated series, the CFPSG and CFPSE exhibited distinct behaviors. The greatest D_{max}/D_0 in the CFPSE case results from the asymmetric spreading to redistribute the momentum and mass of the droplet. Conversely, the CFPSG exhibited the smallest D_{max}/D_0, consistent with the findings of previous studies about the impact between droplets and soft solid.[12−16] In reference to these previous studies, if the natural frequency of a flexible surface is lower than that of the spreading droplet, the downward movement of the surface will proceed throughout the entire spreading phase of the droplet to reduce the relative impacting velocity and load, resulting in an obvious D_{max}/D_0 reduction in comparison to a rigid case. However, if the natural frequency of a flexible surface is greater, the surface will reach its maximum deformation before the maximum spread of the droplet, yielding a minimal D_{max}/D_0 reduction with the assistance of viscoelastic breaking from soft materials.[36] However, the small difference in D_{max}/D_0 between the flexible CFPSG and the rigid CRSG cannot be solely ascribed to viscoelastic breaking. As mentioned previously (see vi, Figure 3c), the wetting within the contacting grids is another source.

With a view to further exploring how the flexibility of grids can affect the spreading behavior of impinging droplets, we established a theoretical model based on energy conservation to estimate the work done W in spreading (see Figures 4b and S9), yielded as

$$W = W_k + W_s + W_p \tag{1}$$

$$\begin{cases} W_k = \dfrac{\pi \rho D_0{}^3 V_0{}^2}{12} \\[3mm] W_s = \pi \sigma D_0{}^2 - \dfrac{\pi \sigma (1 - \cos\theta) D_{max}{}^2}{4} \qquad \text{rigid case} \\[3mm] W_p = \dfrac{\pi \rho g D_0{}^3}{6}\left(\dfrac{D_0}{2} - \dfrac{D_0{}^3}{3 D_{max}{}^2}\right) \end{cases} \tag{2}$$

$$\begin{cases} W_k = \dfrac{\pi \rho D_0{}^3 V_0{}^2}{12} \\[3mm] W_s = \pi \sigma D_0{}^2 - \dfrac{\pi \sigma (1 - \cos\theta) D_{max}{}^2 \sqrt{(\delta/p)^2 + 1/4}}{2} \\[3mm] W_p = \dfrac{\pi \rho g D_0{}^3}{6}\left(\dfrac{D_0}{2} - \dfrac{2 D_{max}\delta}{3p} + \delta \right. \\[3mm] \qquad\quad \left. - \dfrac{D_0{}^3}{6 D_{max}{}^2 \sqrt{(\delta/p)^2 + 1/4}}\right) - \dfrac{\alpha \pi k \delta^2 p^2}{24} \end{cases} \tag{3}$$

flexible case

Here, the subitems W_k, W_s, and W_p correspond to kinetic energy, surface energy, and potential energy, respectively. θ is the apparent contact angle, g is the gravitational acceleration, p is the cell pitch, δ is the deformation of cell center, k is the stiffness of cell center, and α is the fraction of grids in a cell. Using this model, we calculated the value of W (see Figures 4c and S10a). In the flexible model, the values of k and δ were obtained from a load−displacement mechanics simulation (see Figure S7). In comparison to the RSG and CRSG, the spreading droplets dissipated more energy on the FPSG and CFPSG, which can be used to verify the reduced restitution coefficient in the next section. Of note, the rigid model overstated the energy consumption in the spreading phase in comparison to the flexible model (see Figure S10b).

3.3.3. Restitution Coefficient. Figure 4d presents the restitution coefficient H_{max}/H as a function of We to quantify the remaining energy of bouncing droplets, regardless of any mass loss arising from partial bouncing or split bouncing. Herein, H is the releasing height of a droplet, and H_{max} is the maximum bouncing height (defined as the distance from the surface to the lowermost rim of the largest rebounded satellite, iv, Figure 3b). For each surface, the restitution coefficient monotonically decreased as We increased, indicating an intensified droplet impalement and an increased energy consumption. The CFPSG exhibited smaller restitution coefficients than the rigid surfaces (CRSG, CRSE, and CSS) due to greater energy consumption when the droplet spread and retracted over the flexible grids. Moreover, the CFPSE showed the smallest restitution coefficients because of its atypical takeoff with an incomplete retraction, thereby avoiding or reducing energy dissipation in the retracting phase.

3.3.4. Contact Time. Figure 4e shows the influence of a flexibility-pattered setting on contact time T_c that is non-

dimensionalized by a timescale τ expressed as $(0.125\rho D_0^3/\sigma)^{0.5}$.[5] Most prior studies have reported a contact time value greater than the theoretical limit of 2.2τ, which can be obtained by balancing inertial and capillary forces, sufficiently exceeding the freezing time to prevent anti-icing. Since the work of Bird et al.,[6] researchers have fabricated embossed microtextures on surfaces to introduce asymmetry into the retracting phase to split impinging droplets,[7,9−11] thereby creating additional retracting centers to reduce the distances between the centers and their respective rims (so as to achieve a measurable reduction in contact time). Also, even without droplet splitting, the asymmetric spreading and retracting induced by macro-curvatures can still ensure an effective contact time reduction by redistributing the momentum and mass of impinging droplets.[8] Meanwhile, inspired by natural leaves and wings, researchers have bypassed the rigid precondition and proposed a flexibility-based strategy to accelerate droplet bouncing with an incomplete retraction due to structural oscillations at impact.[12−20] Our flexibility-patterned arrangement devotes a rigidity−flexibility hybrid solution to combine the above two mechanisms, paving the way for overcoming the strict requirement related to impacting positioning.

For the CSS, the contact time increased as We increased but had a V-shaped rebound when We exceeded ∼44.07. Note that when We was greater than ∼30.63, the CSS exhibited a partial bouncing (see Figure 3a), so that its contact time was calculated for the rebounding satellite, regardless of the pinning part. Accordingly, the above V-shaped rebound of contact time can be ascribed to the "stick-slip" effect. More precisely, a partial pinning will delay the bouncing time; this delay effect becomes stronger when the partial pinning intensifies as We increases; when the pinning part is large enough in relation to the bouncing satellite, its splitting action will significantly reduce the mass of the bouncing satellite, inducing a sharp reduction in contact time; the first two steps were repeated to yield contact time growth again. The CRSG exhibited a shorter contact time than the CSS, indicating a contact time reduction powered by a grid topology. In comparison to the CRSG, the CFPSG reduced the contact time, while the decreasing amplitude was limited by confined oscillation and partial wetting for the flexible grids, which have been highlighted by the bouncing type described previously (see vi, Figure 3c). Interestingly, and thanks to the asymmetric redistribution (see vii, Figure 3c), the CFPSE exhibited an obvious reduction in contact time even to break through the inertial−capillary limit. Moreover, even without the deforma-tion of flexible grids to yield a convex curvature, the CRSE also presented a measurable contact time reduction, which can be attributed to the asymmetric redistribution solely caused by rigid edges, like the embossed stripes did in previous studies.[6,7,9−11] Note that when the volume of impacting droplets was reduced from 8 to 0.5 μL, there was no obvious difference of contact time among the fabricated surfaces. Namely, in the CFPSG and CRSG cases, the structural oscillation mechanism was limited by confined oscillation and partial wetting for the flexible grids, and in the CFPSE and CRSE cases, the asymmetric redistribution mechanism was not triggered due to the small droplet size with respect to the rigid edges.

3.4. Liquid Evaporation. Besides the liquid-repelling application discussed above, we used a micropipette to generate water droplets to lightly touch the surfaces, with a view to gauging evaporation application (see Movie S6). As

soon as the droplet contacted the SS, it spread rapidly in a radial manner and was eventually trapped by the surface, highlighting the inherent hydrophilicity of the UTL resin. The droplet exhibited a mild symmetrical spreading after contacting the FPSG but underwent a mild asymmetrical spreading after touching the FPSE and finally beaded up atop the grids and edges instead of conforming to the substrate, consistent with the static repellency mentioned in Section 3.2. To accelerate evaporation, we used wipes (Kimtech, USA) to absorb the droplets. The droplets trapped on the FPSG and FPSE were easier to be absorbed than that on the SS, highlighting better liquid repellency. After the absorption, the residual water on the FPSG and FPSE was much faster to vanish than that on the SS, indicating the enhanced evaporating ability created by the grid topology via increasing the roughness and reducing the fraction of solid−liquid interface. In comparison to the FPS, similar phenomena can be observed on the RS but can be distinguished in the evaporation of residual water. More precisely, the FPSG deformed due to the surface tension of residual water but restored as the water evaporated; however, the RSG remained unchanged during the wetting and evaporating phases due to the rigidity of the HTL resin. The above deforming and restoring actions of the FPSG can be more clearly seen on a defective FPSG (see Movie S7). In contrast with the FPS case, for the CFPS, we were required to drop a droplet from the micropipette at a very low velocity because the droplet cannot be directly trapped by the surface. This droplet was the easiest to be absorbed and was the fastest to be thoroughly evaporated, thus indicating an additional improvement afforded by the low-surface-energy chemical modification.

4. CONCLUSIONS

In summary, we have bridged the gap between two scientific strategies (i.e., rigidity-based asymmetric redistribution and flexibility-based structural oscillation) of designing artificial surfaces in liquid-repelling applications. In analogy to a trampoline park, we designed a FPS with flexible cells barred by rigid edges and used three-dimensional projection micro-stereolithography to precisely replicate our design. In contrast to the single-mechanism approaches described in previous works, the flexibility-patterned design is of great significance because it paves the way for tuning droplet bouncing through a synergistic mechanism, that is, contact time reduction is envisioned to be respectively triggered by asymmetric redistribution and structural oscillation mechanisms when the droplet−solid impact occurs on rigid edges and flexible cells, thereby overcoming the strict requirement on impacting positioning. The FPS is shown to achieve a contact time reduction through the structural oscillation mechanism and even to break through the theoretical inertial−capillary limit due to the asymmetric redistribution mechanism. Furthermore, our flexibility-patterned design is also shown to yield 21.23 and 14.17% improvements of droplet impalement resistance through the structural oscillation and asymmetric redistrib-ution mechanisms, respectively. We believe this study to be the first demonstration of the synergistic effect obtained by a hybrid strategy that exploits rigidity-based asymmetric redistribution and flexibility-based structural oscillation in liquid-repelling applications, providing an unprecedented level of control over wettability. Since its beginning, studies on the droplet−solid impact have entered into a rigidity−flexibility cooperative mode, thus broadening the way of wettability

tuning. Besides, the FPS is also applied to accelerate liquid evaporation. As an outlook, an introduction of flexibility gradients will trigger a window of opportunity for more new functionalities and possibilities. For instance, if a flexibility gradient can be created by setting a different flexibility to the patterned flexible cells on the surface, it is possible to directionally rebound droplets for droplet transport.[21] In addition, although the three-dimensional printing is possible to replicate our design for a large-scale fabrication,[23,24,32,37,38] a facile and economical fabrication process is still required for a mass production, for example, using the printer to produce sacrificial molds made of rigid resins and copying the topology with common soft materials such as polydimethylsiloxane.[39]

ASSOCIATED CONTENT

ⓢ Supporting Information

The Supporting Information is available free of charge at https://pubs.acs.org/doi/10.1021/acsami.1c05243.

> Additional details about surface design and fabrication, static liquid repellency, kinetic liquid repellency, and evaporation (PDF)
> Compression test (MP4)
> Contact angle and adhesion (MP4)
> Impalement resistance of uncoated surfaces (MP4)
> Impalement resistance of coated surfaces (MP4)
> Structural oscillation at impact (MP4)
> Evaporation (MP4)
> Deforming and restoring behaviors of flexible grids (MP4)

AUTHOR INFORMATION

Corresponding Authors

Xi Shi − *State Key Laboratory of Mechanical System and Vibration, Shanghai Jiao Tong University, Shanghai 200240, China*; Email: xishi@sjtu.edu.cn

Zhike Peng − *State Key Laboratory of Mechanical System and Vibration, Shanghai Jiao Tong University, Shanghai 200240, China*; ⓘ orcid.org/0000-0002-2095-7075; Email: z.peng@sjtu.edu.cn

Authors

Songtao Hu − *State Key Laboratory of Mechanical System and Vibration, Shanghai Jiao Tong University, Shanghai 200240, China*; ⓘ orcid.org/0000-0002-8405-3788

Xiaobao Cao − *Department of Chemistry and Applied Biosciences, ETH Zurich, Zurich 8093, Switzerland*; ⓘ orcid.org/0000-0003-2211-2823

Tom Reddyhoff − *Department of Mechanical Engineering, Imperial College London, London SW7 2AZ, U.K.*

Andrew J. deMello − *Department of Chemistry and Applied Biosciences, ETH Zurich, Zurich 8093, Switzerland*

Daniele Dini − *Department of Mechanical Engineering, Imperial College London, London SW7 2AZ, U.K.*; ⓘ orcid.org/0000-0002-5518-499X

Complete contact information is available at:
https://pubs.acs.org/10.1021/acsami.1c05243

Author Contributions

∥S.H. and X.C. contributed equally to this work.

Notes

The authors declare no competing financial interest.

ACKNOWLEDGMENTS

REFERENCES

(1) Schutzius, T. M.; Jung, S.; Maitra, T.; Graeber, G.; Köhme, M.; Poulikakos, D. Spontaneous Droplet Trampolining on Rigid Superhydrophobic Surfaces. *Nature* **2015**, *527*, 82−85.

(2) Wang, D.; Sun, Q.; Hokkanen, M. J.; Zhang, C.; Lin, F.-Y.; Liu, Q.; Zhu, S.-P.; Zhou, T.; Chang, Q.; He, B.; Zhou, Q.; Chen, L.; Wang, Z.; Ras, R. H. A.; Deng, X. Design of Robust Superhydrophobic Surfaces. *Nature* **2020**, *582*, 55−59.

(3) Minemawari, H.; Yamada, T.; Matsui, H.; Tsutsumi, J. y.; Haas, S.; Chiba, R.; Kumai, R.; Hasegawa, T. Inkjet Printing of Single-Crystal Films. *Nature* **2011**, *475*, 364−367.

(4) Xu, W.; Zheng, H.; Liu, Y.; Zhou, X.; Zhang, C.; Song, Y.; Deng, X.; Leung, M.; Yang, Z.; Xu, R. X.; Wang, Z. L.; Zeng, X. C.; Wang, Z. A Droplet-Based Electricity Generator with High Instantaneous Power Density. *Nature* **2020**, *578*, 392−396.

(5) Richard, D.; Clanet, C.; Quéré, D. A Contact Time of a Bouncing Drop. *Nature* **2002**, *417*, 811.

(6) Bird, J. C.; Dhiman, R.; Kwon, H.-M.; Varanasi, K. K. Reducing the Contact Time of a Bouncing Drop. *Nature* **2013**, *503*, 385−388.

(7) Gauthier, A.; Symon, S.; Clanet, C.; Quéré, D. Water Impacting on Superhydrophobic Macrotextures. *Nat. Commun.* **2015**, *6*, 8001.

(8) Liu, Y.; Andrew, M.; Li, J.; Yeomans, J. M.; Wang, Z. Symmetry Breaking in Drop Bouncing on Curved Surfaces. *Nat. Commun.* **2015**, *6*, 10034.

(9) Shen, Y.; Tao, J.; Tao, H.; Chen, S.; Pan, L.; Wang, T. Approaching the Theoretical Contact Time of a Bouncing Droplet on the Rational Macrostructured Superhydrophobic Surfaces. *Appl. Phys. Lett.* **2015**, *107*, 111604.

(10) Song, M.; Liu, Z.; Ma, Y.; Dong, Z.; Wang, Y.; Jiang, L. Reducing the Contact Time Using Macro Anisotropic Superhydrophobic Surfaces - Effect of Parallel Wire Spacing on the Drop Impact. *NPG Asia Mater.* **2017**, *9*, No. e415.

(11) Hu, S.; Reddyhoff, T.; Puhan, D.; Vladescu, S.-C.; Shi, X.; Dini, D.; Peng, Z. Droplet Manipulation of Hierarchical Steel Surfaces Using Femtosecond Laser Fabrication. *Appl. Surf. Sci.* **2020**, *521*, 146474.

(12) Vasileiou, T.; Gerber, J.; Prautzsch, J.; Schutzius, T. M.; Poulikakos, D. Superhydrophobicity Enhancement through Substrate Flexibility. *Proc. Natl. Acad. Sci. U.S.A.* **2016**, *113*, 13307−13312.

(13) Weisensee, P. B.; Tian, J.; Miljkovic, N.; King, W. P. Water Droplet Impact on Elastic Superhydrophobic Surfaces. *Sci. Rep.* **2016**, *6*, 30328.

(14) Vasileiou, T.; Schutzius, T. M.; Poulikakos, D. Imparting Icephobicity with Substrate Flexibility. *Langmuir* **2017**, *33*, 6708−6718.

(15) Kim, J.-H.; Rothstein, J. P.; Shang, J. K. Dynamics of a Flexible Superhydrophobic Surface during a Drop Impact. *Phys. Fluids* **2018**, *30*, 072102.

(16) Chantelot, P.; Coux, M.; Clanet, C.; Quéré, D. Drop Trampoline. *Europhys. Lett.* **2018**, *124*, 24003.

(17) Wang, L.; Gong, Q.; Zhan, S.; Jiang, L.; Zheng, Y. Robust Anti-Icing Performance of a Flexible Superhydrophobic Surface. *Adv. Mater.* **2016**, *28*, 7729−7735.

(18) Wang, L.; Gao, C.; Hou, Y.; Zheng, Y.; Jiang, L. Magnetic Field-Guided Directional Rebound of a Droplet on a Superhydrophobic Flexible Needle Surface. *J. Mater. Chem. A* **2016**, *4*, 18289−18293.

(19) Wang, L.; He, Z.; Ding, Y.; Zhou, X.; Liu, J. The Rebound Motion of Liquid Metal Droplet on Flexible Micro/Nano Needle Forest. *Adv. Mater. Interfaces* **2016**, *3*, 1600008.

(20) Hu, S.; Cao, X.; Reddyhoff, T.; Puhan, D.; Vladescu, S.-C.; Wang, J.; Shi, X.; Peng, Z.; deMello, A. J.; Dini, D. Liquid Repellency Enhancement through Flexible Microstructures. *Sci. Adv.* **2020**, *6*, No. eaba9721.

(21) Sun, Q.; Wang, D.; Li, Y.; Zhang, J.; Ye, S.; Cui, J.; Chen, L.; Wang, Z.; Butt, H.-J.; Vollmer, D.; Deng, X. Surface Charge Printing for Programmed Droplet Transport. *Nat. Mater.* **2019**, *18*, 936−941.

(22) Wen, J.; Reddyhoff, T.; Hu, S.; Puhan, D.; Dini, D. Exploiting Air Cushion Effects to Optimise a Superhydrophobic/Hydrophilic Patterned Liquid Ring Sealed Air Bearing. *Tribol. Int.* **2020**, *144*, 106129.

(23) Xiang, Y.; Huang, S.; Huang, T.-Y.; Dong, A.; Cao, D.; Li, H.; Xue, Y.; Lv, P.; Duan, H. Superrepellency of Underwater Hierarchical Structures on Salvinia Leaf. *Proc. Natl. Acad. Sci. U.S.A.* **2020**, *117*, 2282−2287.

(24) Feng, S.; Delannoy, J.; Malod, A.; Zheng, H.; Quéré, D.; Wang, Z. Tip-induced Flipping of Droplets on Janus Pillars: From Local Reconfiguration to Global Transport. *Sci. Adv.* **2020**, *6*, No. eabb4540.

(25) Hu, S.; Cao, X.; Reddyhoff, T.; Puhan, D.; Vladescu, S.-C.; Wang, Q.; Shi, X.; Peng, Z.; deMello, A. J.; Dini, D. Self-Compensating Liquid-Repellent Surfaces with Stratified Morphology. *ACS Appl. Mater. Interfaces* **2020**, *12*, 4174−4182.

(26) Hensel, R.; Finn, A.; Helbig, R.; Braun, H.-G.; Neinhuis, C.; Fischer, W.-J.; Werner, C. Biologically Inspired Omniphobic Surfaces by Reverse Imprint Lithography. *Adv. Mater.* **2014**, *26*, 2029−2033.

(27) Feng, L.; Zhang, Y.; Xi, J.; Zhu, Y.; Wang, N.; Xia, F.; Jiang, L. Petal Effect: A Superhydrophobic State with High Adhesive Force. *Langmuir* **2008**, *24*, 4114−4119.

(28) Long, J.; Fan, P.; Gong, D.; Jiang, D.; Zhang, H.; Li, L.; Zhong, M. Superhydrophobic Surfaces Fabricated by Femtosecond Laser with Tunable Water Adhesion: from Lotus Leaf to Rose Petal. *ACS Appl. Mater. Interfaces* **2015**, *7*, 9858−9865.

(29) Li, X.; Wang, J.; Zhao, Y.; Zhang, X. Template-Free Self-Assembly of Fluorine-Free Hydrophobic Polyimide Aerogels with Lotus or Petal Effect. *ACS Appl. Mater. Interfaces* **2018**, *10*, 16901−16910.

(30) Hensel, R.; Helbig, R.; Aland, S.; Voigt, A.; Neinhuis, C.; Werner, C. Tunable Nano-Replication to Explore the Omniphobic Characteristics of Springtail Skin. *NPG Asia Mater.* **2013**, *5*, No. e37.

(31) Hu, S.; Reddyhoff, T.; Puhan, D.; Vladescu, S.-C.; Huang, W.; Shi, X.; Dini, D.; Peng, Z. Bi-Gaussian Stratified Wetting Model on Rough Surfaces. *Langmuir* **2019**, *35*, 5967−5974.

(32) Liu, X.; Gu, H.; Wang, M.; Du, X.; Gao, B.; Elbaz, A.; Sun, L.; Liao, J.; Xiao, P.; Gu, Z. 3D Printing of Bioinspired Liquid Superrepellent Structures. *Adv. Mater.* **2018**, *30*, 1800103.

(33) Liu, Y.; Moevius, L.; Xu, X.; Qian, T.; Yeomans, J. M.; Wang, Z. Pancake Bouncing on Superhydrophobic Surfaces. *Nat. Phys.* **2014**, *10*, 515−519.

(34) Bro, J. A.; Jensen, K. S. B.; Larsen, A. N.; Yeomans, J. M.; Hecksher, T. The Macroscopic Pancake Bounce. *Eur. J. Phys.* **2017**, *38*, 015006.

(35) Soto, D.; De Larivière, A. B.; Boutillon, X.; Clanet, C.; Quéré, D. The Force of Impacting Rain. *Soft Matter* **2014**, *10*, 4929−4934.

(36) Rioboo, R.; Voué, M.; Adão, H.; Conti, J.; Vaillant, A.; Seveno, D.; De Coninck, J. Drop Impact on Soft Surfaces: Beyond the Static Contact Angles. *Langmuir* **2010**, *26*, 4873−4879.

(37) Tricinci, O.; Terencio, T.; Mazzolai, B.; Pugno, N. M.; Greco, F.; Mattoli, V. 3D Micropatterned Surface Inspired by Salvinia Molesta via Direct Laser Lithography. *ACS Appl. Mater. Interfaces* **2015**, *7*, 25560−25567.

(38) Hu, S.; Cao, X.; Reddyhoff, T.; Puhan, D.; Huang, W.; Shi, X.; Peng, Z.; Dini, D. Three-Dimensional Printed Surfaces Inspired by Bi-Gaussian Stratified Plateaus. *ACS Appl. Mater. Interfaces* **2019**, *11*, 20528−20534.

(39) de Marco, C.; Alcântara, C. C. J.; Kim, S.; Briatico, F.; Kadioglu, A.; de Bernardis, G.; Chen, X.; Marano, C.; Nelson, B. J.; Pané, S. Indirect 3D and 4D Printing of Soft Robotic Microstructures. *Adv. Mater. Technol.* **2019**, *4*, 1900332.